Microchemical Journal 221 (2026) 116819

Contents lists available at ScienceDirect

Microchemical Journal

journal homepage: www.elsevier.com/locate/microc

In_2O_3/Bi_2WO_6 heterojunction based photoelectrochemical biosensor for *Burkholderia pseudomallei* DNA detection

Ye Zhao [a,b], Yiyong Wang [a], Chen Yuan [b], Yu Xiao [c], Qianfeng Xia [a,*], Huangxian Ju [b,*]

[a] NHC Key Laboratory of Tropical Disease Control, School of Life Sciences and Medical Technology, Hainan Medical University, Haikou, Hainan 571199, China
[b] State Key Laboratory of Analytical Chemistry for Life Science, School of Chemistry and Chemical Engineering, Nanjing University, Nanjing 210023, China
[c] Department of Medical Laboratory, Affiliated Hospital of Southwest Medical University, Luzhou 646000, China

ARTICLE INFO

Keywords:
Burkholderia pseudomallei
Photoelectrochemistry
Biosensors
In_2O_3/Bi_2WO_6 heterojunction
DNA analysis

ABSTRACT

Burkholderia pseudomallei is a causative agent of melioidosis, a severe tropical infectious disease characterized by high mortality rate and zoonotic potential. However current methods for detecting *B. pseudomallei* face the challenges of sensitivity and simplicity. In this work, an In_2O_3/Bi_2WO_6 heterojunction was synthesized via a hydrothermal method to construct a highly sensitive photoelectrochemical (PEC) sensor for accurate detection of *Burkholderia pseudomallei* DNA. Under visible light excitation, the heterojunction could effectively facilitate the electron-hole separation for significantly enhancing the PEC performance. The In_2O_3/Bi_2WO_6 heterojunction exhibited 5-fold stronger PEC signal than pure Bi_2WO_6, thus providing a basis for "on-off" photoelectrochemical biosensing. By target DNA-triggered catalyzed hairpin assembly (CHA) cascade amplification, abundant G-quadruplex/hemin DNAzyme structures could be formed on magnetic beads, which then catalyzed the oxidation of 4-chloro-1-naphthol by H_2O_2 to produce insoluble benzo-4-chloro-hexadienone. After the resulting precipitate was deposited on the In_2O_3/Bi_2WO_6-modified ITO surface, the electron transfer in the PEC process was inhibited, which caused a marked decrease in the photocurrent response for target DNA detection. The proposed method exhibited a broad detection range of 1.0 nM to 1.0 fM for *B. pseudomallei* DNA along with a detection limit of 0.17 fM and satisfactory recoveries (91.4–108.5 %) in real serum sample analysis, indicating the promising application of the synthesized heterojunction and proposed PEC method in ultrasensitive detection of *B. pseudomallei* DNA.

1. Introduction

Melioidosis is a zoonotic infectious disease caused by the gram-negative bacterium *Burkholderia pseudomallei* (*B. pseudomallei*), which affects both humans and animals, primarily in tropical and subtropical regions [1,2]. *B. pseudomallei* survives for long periods in moist soil and demonstrates strong ecological adaptability, infecting humans and other mammals [3–5]. Its clinical manifestations are highly diverse, earning melioidosis the nickname "the great mimicker" due to its resemblance to other diseases [6]. Annually, there are approximately 165,000 cases worldwide and nearly 89,000 deaths. The incidence is about five cases per 100,000 individuals in high-risk populations [7–9]. The disease is often severe and difficult to diagnose, requiring sensitive and rapid detection methods. Current methods for detecting *B. pseudomallei* include bacterial culture method, immunoassays (e.g., IHA, ELISA, and IFA), mass spectrometry, chemiluminescence, and electrochemical techniques [5,10]. Among these, bacterial culture is recognized as the "gold standard". However, its sensitivity is only about 60 %, and the culture cycle lasts 2–7 days. This delay fails to meet clinical demand for rapid diagnosis [10]. Moreover, most alternative methods rely on costly equipment, specialized operators, and stringent experimental conditions, thereby limiting their application in grassroots settings and resource-constrained regions. Therefore, it is of utmost importance to develop a highly sensitive, specific, user-friendly method suitable for point-of-care testing.

Photoelectrochemical (PEC) biosensing has attracted extensive attention due to its advantages of high sensitivity, low background, low cost and simple equipment [11,12]. Upon light radiation, photosensitive materials generate electron–hole pairs by exciting electrons from the valence band (VB) to the conduction band (CB). Under the influence of the internal electric field (IEF), the separation of photogenerated carriers facilitates electron transfer between the photoelectrode and the

* Corresponding authors.
E-mail addresses: xiaqianfeng@hainmc.edu.cn (Q. Xia), hxju@nju.edu.cn (H. Ju).

https://doi.org/10.1016/j.microc.2026.116819
Received 22 October 2025; Received in revised form 18 December 2025; Accepted 3 January 2026
Available online 5 January 2026
0026-265X/© 2026 Elsevier B.V. All rights are reserved, including those for text and data mining, AI training, and similar technologies.

electrolyte, thereby generating a photocurrent [13]. However, the practical use of photosensitive materials is hindered by their limited light-harvesting ability and rapid electron–hole recombination [14,15]. Rational design and fabrication of photosensitive materials are essential for enhancing PEC performance. Among potential candidates, bismuth-based materials, especially Bi_2WO_6, have attracted attention owing to their visible-light response, stability, and environmental compatibility [16–18]. Bi_2WO_6 exhibits orthorhombic symmetry, with its structure composed of alternately arranged $(Bi_2O_2)^{2+}$ layers and $(WO_4)^{2-}$ octahedral layers interconnected through their vertices, which creates an electric field parallel to the (001) plane to facilitate the migration of photogenerated charges within the material [19]. It has been widely applied across various fields, including photocatalysis [20], cancer treatment [21], water purification [22], and PEC sensing [23]. However, the PEC performance of conventional Bi_2WO_6 is inherently limited by the rapid recombination of photogenerated holes with electrons [24,25]. To address these limitations, researchers have developed multiple strategies, including metal or nonmetal doping, noble metal or oxide loading, and heterojunction constructed with two semiconductors [26]. Compared to single semiconductors, such heterojunctions can enhance electron-hole pair separation more effectively, thereby improving PEC performance [27].

Owing to the excellent electrical conductivity, efficient absorption of visible light, and remarkable stability against photocorrosion [28], indium oxide, a typical n-type semiconductor with a bandgap of 2.6–2.8 eV, possesses excellent performance in PEC water splitting, where the (001) crystal plane is conducive to hole accumulation [29]. However, In_2O_3 exhibits low PEC efficiency due to its wide bandgap and rapid electron-hole recombination. In view of the complementary band structures of Bi_2WO_6 and In_2O_3, this work used them to construct a novel In_2O_3/Bi_2WO_6 heterojunction (Scheme 1A). Under intrinsic electric fields, electrons could transfer from the conduction band of In_2O_3 to that of Bi_2WO_6, while holes migrated from Bi_2WO_6 to In_2O_3, leading to facilitated electron-hole separation and significantly enhanced PEC signal. By casting In_2O_3/Bi_2WO_6 heterojunction on ITO electrode to serve as the photoactive matrix and then dropping target DNA-induced product on the In_2O_3/Bi_2WO_6 modified electrode to inhibit the photocurrent signal [30–33], a simple PEC biosensing method was proposed for *B. pseudomallei* DNA (Scheme 1B). The insoluble product, benzo-4-chloro-hexadienone (4-CD), was formed in the presence of target DNA, which triggered the formation of abundant G-quadruplex/hemin DNAzymes with a catalytic hairpin assembly (CHA) on the surface of magnetic beads to catalyze the oxidation of 4-chloro-1-naphthol (4-CN) by H_2O_2. The "on-off" biosensing method provided a valuable technical support for the early diagnosis of melioidosis.

2. Experimental section

2.1. Materials and reagents

The materials and reagents used in this study are presented in the Supporting information. The oligonucleotide sequences were listed in Table S1.

2.2. Preparation of In_2O_3

A total of 3.0 g of urea and 0.5 g of indium chloride tetrahydrate ($InCl_3{\cdot}4H_2O$) were dissolved in 37.5 mL of deionized water and stirred at 80 °C for 14 h (Scheme 1A). After naturally cooling to room temperature, the resulting suspension was centrifuged at 8000 rpm and washed three times with absolute ethanol and deionized water, respectively. The obtained white precipitate was dried under vacuum at 60 °C for 12 h. The dried powder was then calcined in air at 700 °C for 5 h with a heating rate of 5 °C/min to obtain yellow rod-like In_2O_3 powder.

2.3. Preparation of In_2O_3/Bi_2WO_6

Firstly, 20 mg of In_2O_3 was dispersed in a mixture of 30 mL of ethanol and 15 mL of deionized water via ultrasonication for 10 min, followed by stirring for 20 min. Under vigorous stirring, 0.0361, 0.0961, 0.144, 0.216 or 0.576 mmol of bismuth nitrate and 0.018, 0.0479, 0.0722, 0.108 or 0.288 mmol of sodium tungstate were added into the suspension for obtaining the optimal PEC performance of In_2O_3/Bi_2WO_6 modified electrode in 0.01 M PBS (pH 7.4) containing 0.1 M ascorbic acid (AA) at 0 V (vs. Ag/AgCl). Accordingly, the molar ratios of In_2O_3 to Bi_2WO_6 in the obtained composites (InO/BWO-1 to InO/BWO-5) were 1:0.25, 1:0.66, 1:1, 1:1.5, and 1:4, respectively. The mixture was sonicated for 10 min and stirred for 2 h (Scheme 1A). Subsequently, 240 mg of NH_4Cl (4 mM) and 0.6 mL of ammonia solution (28 %) were added. The resulting solution was transferred into a 100 mL Teflon-lined stainless steel autoclave and heated at 180 °C for 6 h. After the reaction, the In_2O_3/Bi_2WO_6 composite was collected by centrifugation,

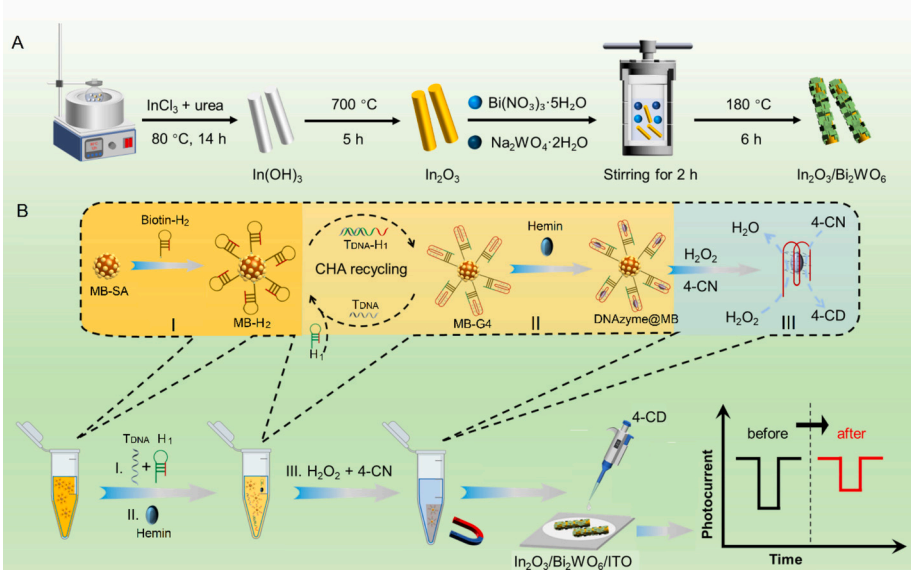

Scheme 1. (A) Schematic illustration of In_2O_3/Bi_2WO_6 preparation, and (B) photoelectrochemical bioassay procedure for T_{DNA} based on CHA mediated enzymatic reaction.

washed three times with ethanol and deionized water, and then dried under vacuum at 60 °C for 12 h.

2.4. Apparatus and data acquisition

The morphology and microstructure were characterized by scanning electron microscopy (SEM, JSM-7800F) and a transmission electron microscope (TEM , JEM-2100). Crystalline structure and phase composition were determined using a Bruker D8 Advance X-ray diffractometer with Cu Kα radiation (40 kV, 40 mA). UV–vis diffuse reflectance spectra (UV–vis DRS) were collected on a UV-3600 spectrophotometer equipped with an integrating sphere, with $BaSO_4$ serving as the reflectance standard. X-ray photoelectron spectroscopy (XPS) was carried out on a PHI 5000 spectrometer, and all binding energies were referenced to the C 1 s peak at 284.8 eV. Electrochemical characterization including Mott–Schottky (M–S) analysis was performed in 0.5 M Na_2SO_4 using a DH7000 electrochemical workstation. The electrochemical impedance spectra (EIS) were recorded in 0.1 M KCl containing 5 mM $K_3Fe(CN)_6/K_4Fe(CN)_6$ (1:1), with a 10 mV amplitude over a range from 0.1 Hz to 10 kHz. Transient photocurrent responses were recorded on a CHI 630D electrochemical workstation under illumination from a 10 W LED lamp with an emission wavelength around 365–370 nm. A standard three-electrode configuration was employed, consisting of a modified indium tin oxide (ITO) working electrode, a platinum wire counter electrode, and an Ag/AgCl reference electrode.

2.5. Construction of sensor and PEC measurement

The PEC sensing procedure was illustrated in Scheme 1B. After the ITO electrodes were sequentially cleaned by ultrasonic treatment in ethanol and deionized water for 30 min each, rinsed with ethanol, and dried under a nitrogen stream, the sensors were prepared by drop-cast 20 μL of In_2O_3/Bi_2WO_6 dispersion (1 mg/mL) on ITO electrodes and dried at room temperature. For the preparation of the MB–H_2 complexes, 30 μL of streptavidin-coated magnetic beads (10 mg/mL) were washed twice with 200 μL washing buffer (1.0 M KCl, 10 mM Tris–HCl, and 1.0 mM EDTA, pH 7.4) and incubated with 100 μL of 0.2 μM biotin-labelled hairpin DNA2 (H_2) at room temperature (20 rpm) for 30 min. The resulting MB–H_2 complexes were separated magnetically, washed twice with 10 mM Tris–HCl buffer (pH 7.4), and stored at 4 °C.

The PEC detection was performed by mixing 10 μL target DNA (T_{DNA}) of various concentrations with 20 μL MB–H_2, 20 μL hairpin DNA1 (H_1, 0.2 μM), 10 μL $MgCl_2$ (50 mM in 10 mM Tris–HCl , pH 7.4), and 40 μL Tris–HCl buffer (10 mM, pH 7.4) in 200 μL centrifuge tubes to achieve the target-induced catalytic hairpin assembly (CHA) by incubating at 37 °C (20 rpm) for 2 h. After magnetic separation and washing, the MBs–complexes were mixed with Tris–HCl buffer (10 mM, pH 7.4) containing 2 μM hemin, 5 mM $MgCl_2$, and 20 mM KCl, and incubated at 37 °C for 40 min to form the G-quadruplex/hemin DNAzyme. Subsequently, 0.02 mM H_2O_2 and 1.0 mM 4-chloro-1-naphthol (4-CN) were added and reacted at room temperature for 10 min to catalyze the formation of insoluble benzo-4-chloro-hexadienone (4-CD). After magnetic separation, 10 μL of the resulting 4-CD-containing mixture was dropped on the sensor and air-dried for PEC measurements, which were carried out in 0.01 M PBS (pH 7.4) containing 0.1 M ascorbic acid (AA) at 0 V (vs. Ag/AgCl).

2.6. Optimization of detection conditions for PEC sensing

The loading amount of hairpin H_2 was optimized by immobilizing 0.1 to 0.5 μM of hairpin H_2 on streptavidin coated magnetic beads to measure the final PEC responses of 1 nM target DNA (T_{DNA}) after target DNA-induced product was dropped on In_2O_3/Bi_2WO_6 modified electrode. The incubation time for CHA was optimized with 0.5, 1.0, 1.5, 2.0, and 2.5 h to examine the change of photocurrent resulted from the target DNA-induced product.

3. Results and discussion

3.1. Characterization of synthesized materials

Scanning electron microscopy (SEM) was used to characterize the morphology of the synthesized In_2O_3/Bi_2WO_6. The precursor $In(OH)_3$ precipitate showed a rod-like morphology (Fig. 1A). After calcination at 700 °C for 5 h in a tube furnace, the obtained In_2O_3 exhibited uniformly aligned nanorods with lengths of approximately 1.5–2 μm (Fig. 1B). Upon growth of Bi_2WO_6 on In_2O_3 nanorods, the obtained In_2O_3/Bi_2WO_6 composite exhibited uniform adhesion of flower-like Bi_2WO_6 nanosheets with an overall diameter of about 2–2.5 μm (Fig. 1C,D). The synergistic construction of these one-dimensional and two-dimensional nanostructures significantly increased the specific surface area. To further elucidate the microstructural feature and interfacial characteristic of the composite, transmission electron microscopic (TEM) and high-resolution TEM (HR-TEM) analyses were performed. The TEM image confirmed that the Bi_2WO_6 nanosheets were tightly anchored onto the surface of the In_2O_3 nanorods, indicating intimate interfacial contact between the two components (Fig. 1E). The HR-TEM image revealed well resolved lattice fringes originating from both phases across the interface without obvious gaps (Fig. 1F), demonstrating the formation of a tightly coupled heterojunction. The interplanar spacing of approximately 0.443 nm could be assigned to the (211) plane of In_2O_3, while another set of lattice fringes with a spacing of about 0.313 nm corresponded to the (113) plane of Bi_2WO_6. The coexistence of distinct lattice fringes at the interface provided direct microscopic evidence for the successful construction of an intimate In_2O_3/Bi_2WO_6 heterojunction, which was highly beneficial for efficient interfacial charge separation and transfer. X-ray diffraction (XRD) was then used to analyze the crystal structures of the obtained In_2O_3, Bi_2WO_6 and In_2O_3/Bi_2WO_6.The diffraction peaks of Bi_2WO_6 at 2θ of 28.3°, 32.8°, 47.2°, 55.8° and 58.6° corresponded to its (113), (200), (220), (313) and (226) planes (JCPDS No. 39–0256) (Fig. 1G), respectively. The diffraction peaks at 2θ of 21.4°, 30.5°, 35.4°, 50.9° and 60.5° were related to the (211), (222), (400), (440) and (622) crystal planes of the orthorhombic In_2O_3 (JCPDS No. 71–2195), respectively. The diffraction peaks of In_2O_3/Bi_2WO_6 matched well with those of Bi_2WO_6 and In_2O_3 without additional peaks observed, indicating the successful formation of the In_2O_3/Bi_2WO_6 composite without introducing new phases.

The presence of In, Bi, O, and W in In_2O_3/Bi_2WO_6 was confirmed by the full XPS spectrum (Fig. 1H), which proved the successful synthesis of the photoactive materials, consistent with the energy-dispersion X-ray spectroscopic (EDS) mapping of In_2O_3/Bi_2WO_6 heterojunction (Fig.S1). High resolution XPS spectra provided detailed information on the chemical states of each element (Fig. 2A–D), which was critical for analyzing the electronic structure and photoelectrochemical properties. The In 3d spectrum of In_2O_3/Bi_2WO_6 showed the In $3d_{3/2}$ and $3d_{5/2}$ peaks of pure In_2O_3 at 452.13 and 444.60 eV, respectively (Fig. 2A), corresponding to In^{3+} [34]. In In_2O_3/Bi_2WO_6 composite, these peaks shifted slightly to 452.28 and 444.74 eV, respectively, indicating the change in electronic environment. Notably, the In 3d spectrum of In_2O_3/Bi_2WO_6 showed a $4d_{5/2}$ peak of Bi^{3+} at 442.49 eV, suggesting an electronic interaction between Bi_2WO_6 and In_2O_3, and further confirming the successful formation of the In_2O_3/Bi_2WO_6 composite. The Bi $4f_{7/2}$ and Bi $4f_{5/2}$ peaks of Bi_2WO_6 were observed at 158.84 eV and 164.16 eV (Fig. 2B), which confirmed that Bi existed in the +3 oxidation state, while in In_2O_3/Bi_2WO_6, these peaks shifted slightly to 159.34 eV and 164.68 eV, indicating a change in the local electronic environment of Bi^{3+}.

The W $4f_{7/2}$ and $4f_{5/2}$ peaks of Bi_2WO_6 were observed at 35.10 eV and 37.24 eV (Fig. 2C), corresponding to W^{6+} [35]. In the In_2O_3/Bi_2WO_6, these peaks shifted slightly to 35.56 and 37.71 eV, also reflecting the modifications in the electronic environment. The O 1 s spectrum of In_2O_3 revealed partial dehydration of the surface hydroxyl groups and the presence of adsorbed oxygen owing to high-temperature calcination,

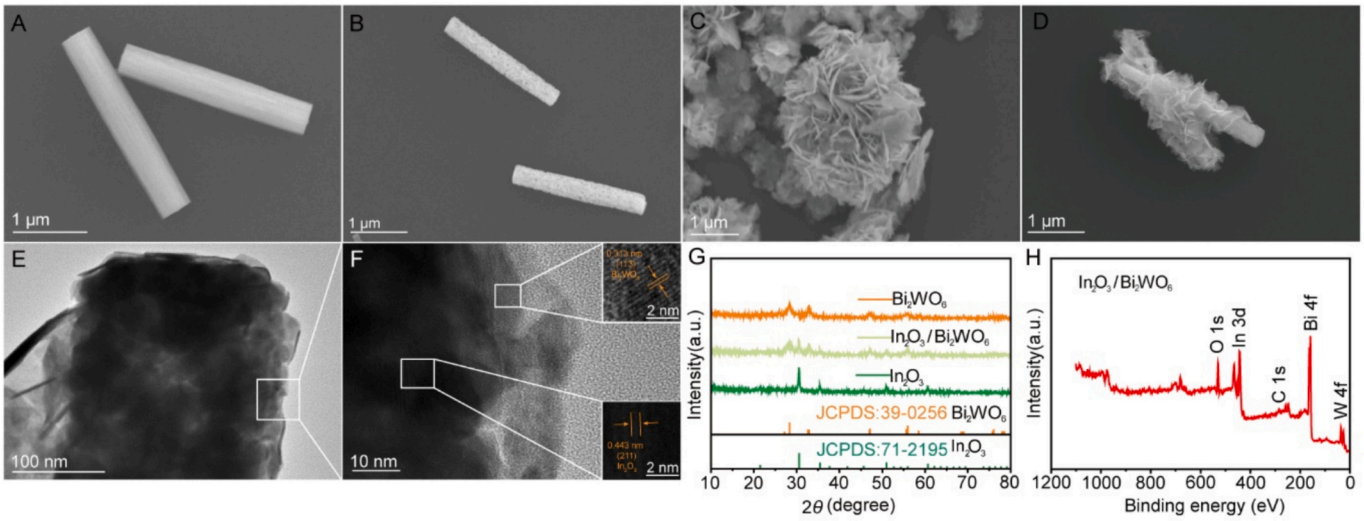

Fig. 1. SEM images of (A) $In(OH)_3$, (B) In_2O_3, (C) Bi_2WO_6, and (D) In_2O_3/Bi_2WO_6. (E) TEM and (F) HR-TEM images of In_2O_3/Bi_2WO_6. (G) XRD patterns of different materials. (F) XPS spectrum of In_2O_3/Bi_2WO_6.

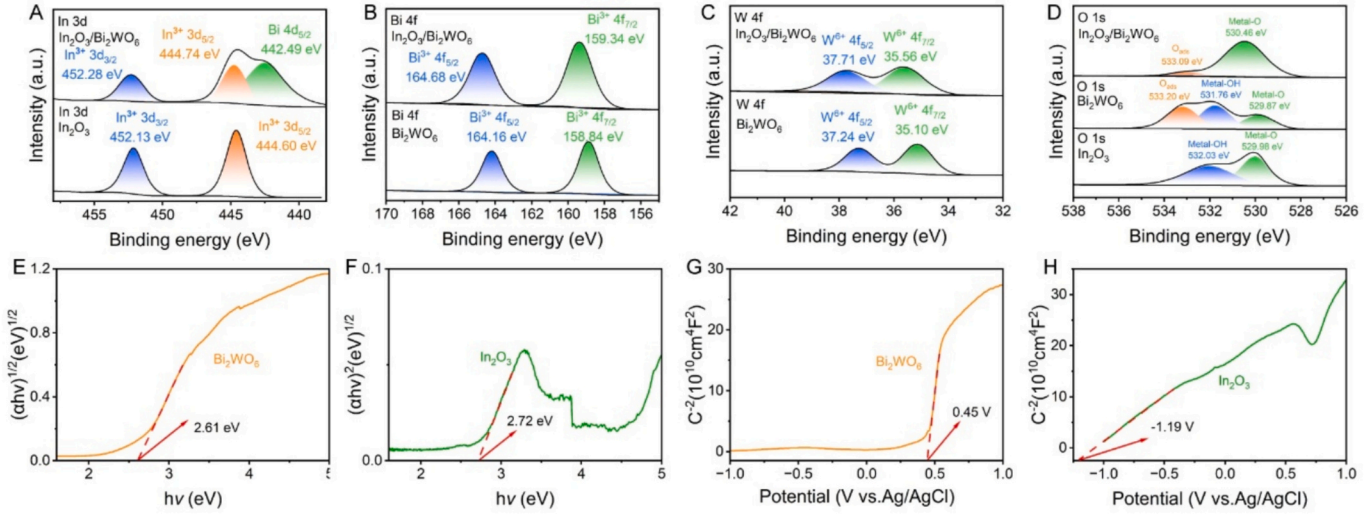

Fig. 2. XPS spectra of (A) In 3d, (B) Bi 4f, (C) W 4f and (D) O 1 s for In_2O_3/Bi_2WO_6. (E,F) UV–Vis diffusion reflectance spectra and (G,H) Mott–Schottky plots of Bi_2WO_6 (E,G) and In_2O_3 (F,H).

with the peaks of metal–oxygen and metal–hydroxyl oxygen at 529.98 and 532.03 eV, respectively (Fig. 2D). In contrast, hydrothermally synthesized Bi_2WO_6 retained more surface hydroxyl and adsorbed oxygen, with peaks at 529.87, 531.76, and 533.20 eV, corresponding to metal–oxygen, M–OH, and adsorbed oxygen, respectively. In In_2O_3/Bi_2WO_6, partial consumption of hydroxyl groups at the interface, possibly due to In–O–Bi bond formation, resulted in the metal–oxygen peak at 530.46 eV and a minor peak of adsorbed oxygen at 533.09 eV. The XPS spectra suggested the partial disappearance of surface hydroxyl groups and the emergence of a modified metal–oxygen peak in In_2O_3/Bi_2WO_6, which could be attributed to the formation of interfacial In–O–Bi bonds. The formation of such hetero-metal–oxygen bridges is widely recognized as strong evidence of chemical bonding rather than simple physical mixing between oxides. In—O—Bi bonds can effectively shorten the electron transport pathway at the interface, promote orbital hybridization, and strengthen electronic coupling between the two semiconductors. Therefore, the formation of In—O—Bi bonds not only validated the intimate interfacial contact between In_2O_3 and Bi_2WO_6 but also revealed the structural origin of the improved charge-transfer efficiency. Overall, compared with In_2O_3 and Bi_2WO_6, the binding energies of all elements in In_2O_3/Bi_2WO_6 exhibited noticeable shifts, reflecting electronic interactions between the two components, which might arise from electronic redistribution induced by the intimate interfacial contact. The XPS results further confirmed the successful construction of In_2O_3/Bi_2WO_6 and its expected chemical states, which was expected to influence the subsequent photoelectrochemical performance.

3.2. PEC properties

The Kubelka–Munk (KM) model was used to analyze the diffuse reflectance spectroscopic (DRS) data. The KM model assumes that the incident light produces two components of light flux in the material. One component is absorbed by the material and enters its interior, whereas the other component is reflected outwards. Owing to the simplicity of its calculations and processing, this model is widely used in DRS optical analysis [36]. The successful construction of In_2O_3/Bi_2WO_6 was further supported by the results of the UV–Vis DRS measurement. In_2O_3 exhibited weak UV–visible absorption, primarily between 200 and 240 nm, while Bi_2WO_6 absorbed strongly across 200–450 nm (Fig. S2A). Compared with pure Bi_2WO_6, the In_2O_3/Bi_2WO_6 composite exhibited a

slightly decreased absorption intensity in the visible-light region, which could be attributed to the introduction of wide-band-gap In_2O_3 and the interfacial electronic interactions between two semiconductors. The band gaps (E_g) of the samples were further estimated from the UV–Vis diffuse reflectance spectra using the Kubelka–Munk (KM) function and the corresponding Tauc plots according to $\alpha h\nu = A(h\nu - E_g)^{n/2}$ [37]. The E_g values of Bi_2WO_6 and In_2O_3 were determined to be 2.61 and 2.72 eV, respectively (Fig. 2E,F). Notably, the In_2O_3/Bi_2WO_6 composite exhibited an intermediate band gap of 2.69 eV (Fig. S2B), indicating effective band coupling at the heterojunction interface. Although the overall visible-light absorption of the composite did not increase, the formation of the In_2O_3/Bi_2WO_6 heterojunction was expected to facilitate photogenerated charge separation and suppress electron–hole recombination through the built-in electric field, thereby providing a fundamental basis for the enhanced PEC performance and subsequent band structure analysis.

The Mott–Schottky curves of both In_2O_3 and Bi_2WO_6 exhibited a positive slope, indicating that they were n-type semiconductors [38]. By extrapolating the linear portion of the curves, the flat band voltages for In_2O_3 and Bi_2WO_6 were obtained as −1.19 and 0.45 V (vs. Ag/AgCl) (Fig. 2G,H) or − 0.99 V and 0.65 V vs. standard hydrogen electrode (NHE) [39], respectively. The conduction band (CB) potential of n-type semiconductors is usually approximately 0.1 V lower than the flat band potential. Therefore, the CB potential of In_2O_3 was estimated to be −1.09 V, and that of Bi_2WO_6 was estimated to be 0.55 V (vs. NHE). From $E_{VB} = E_g + E_{CB}$, the valence band (VB) potentials for In_2O_3 and Bi_2WO_6 were calculated to be 1.63 and 3.16 V (vs. NHE), respectively. Therefore, the PEC process could be proposed in Fig. 3A. The favorable energy band alignment between In_2O_3 and Bi_2WO_6 facilitated the formation of a highly efficient heterojunction. In the presence of ascorbic acid (AA) as a sacrificial hole scavenger, which did not participate in the modulation of the band structure of the In_2O_3/Bi_2WO_6 heterojunction, photogenerated holes in the valence bands were readily consumed by AA, which effectively suppressed interfacial electron–hole recombination and promoted charge separation by prolonging the lifetime of photogenerated electrons without altering the intrinsic band alignment or charge transfer pathway of the heterojunction.

Under visible light excitation, photogenerated electrons firstly transited from the VB to CB. Due to the difference in conduction band positions, photo-generated electrons in In_2O_3 could migrate to the conduction band of Bi_2WO_6. Simultaneously, the rod-like In_2O_3 structure provided efficient pathways for hole transport, causing the migration of holes in Bi_2WO_6 to the valence band of In_2O_3, which achieved effective spatial separation, and thus significantly suppressed electron–hole recombination, and extended carrier lifetime. Bi_2WO_6 rapidly accepted the electrons from the conduction band of In_2O_3 through its excellent electron mobility and strong interface coupling, further enhancing the migration efficiency of photo-generated carriers. Therefore, the well-matched band structure effectively promoted carrier migration and enhanced the photoelectrochemical performance of the composite.

3.3. PEC characterization of modified electrode with In_2O_3/Bi_2WO_6

To assess the PEC performance of In_2O_3/Bi_2WO_6, the (photo)electrochemical properties were further examined. From the Nyquist semicircles [33], the In_2O_3/Bi_2WO_6 modified ITO electrode exhibited a markedly reduced charge transfer resistance (R_{ct} = 465.1 Ω) compared

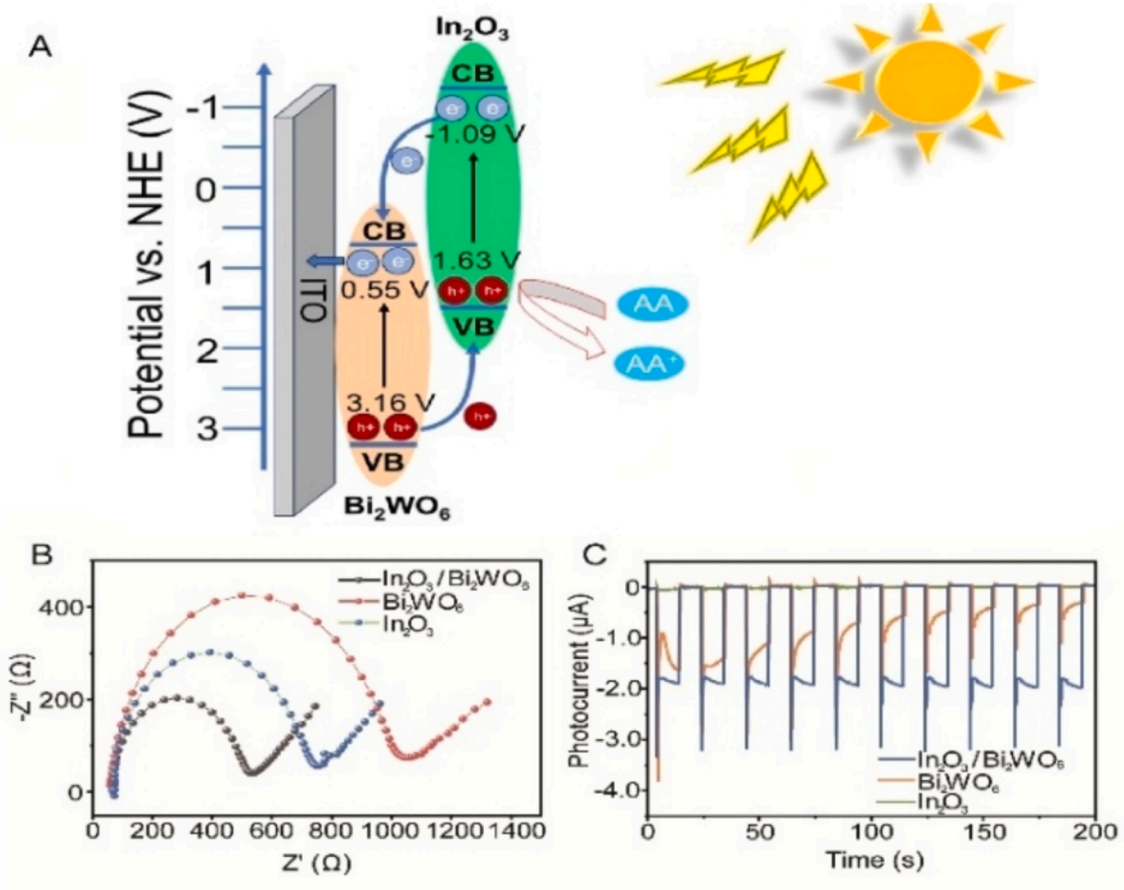

Fig. 3. (A) Scheme for charge transfer mechanism of In_2O_3/Bi_2WO_6/ITO in presence of AA. (B) EIS Nyquist spectra and (C) PEC responses of Bi_2WO_6, In_2O_3 and In_2O_3/Bi_2WO_6 modified ITO electrodes in 0.01 M PBS buffer (pH 7.4) containing 0.1 M AA at 0 V (vs. Ag/AgCl).

with In_2O_3 modified (R_{ct} = 661.4 Ω) and Bi_2WO_6 modified (R_{ct} = 955.6 Ω) ITO electrodes (Fig. 3B), indicating that the heterojunction markedly enhanced electron transport, which greatly increased the transient photocurrent response (Fig. 3C). The In_2O_3/ITO electrode exhibited only a weak response of ~0.02 μA, while Bi_2WO_6/ITO showed a response of ~0.4 μA, demonstrating its superior ability to promote carrier separation and transport under visible-light irradiation. However, the photocurrent of Bi_2WO_6/ITO gradually decayed over time due to rapid electron-hole pair recombination. By contrast, In_2O_3/Bi_2WO_6/ITO exhibited about 5-fold stronger photoelectrochemical signal (~1.9 μA) than Bi_2WO_6/ITO, confirming that the heterojunction accelerated charge transfer and suppresses recombination. It should be noted that the photocurrent of Bi_2WO_6/ITO gradually decayed during continuous illumination due to rapid electron–hole recombination. Therefore, the photocurrent value of Bi_2WO_6/ITO was recorded after 150 s of irradiation, when the signal reached a relatively stable value.

3.4. Feasibility of photoelectrochemical biosensing and condition optimization

To verify the feasibility of In_2O_3/Bi_2WO_6 composite for photoelectrochemical biosensing, a target DNA-triggered catalyzed hairpin assembly (CHA) recycling was used to form abundant G-quadruplex/hemin DNAzyme on magnetic beads (MB) for catalyzing the oxidation of 4-chloro-1-naphthol (4-CN) by H_2O_2, which produced insoluble benzo-4-chloro-hexadienone (4-CD) to inhibit the photocurrent signal of In_2O_3/Bi_2WO_6/ITO (Scheme 1B). The target-activated CHA recycling was demonstrated with native PAGE analysis (Fig. S3). All experiments were conducted in a unified reaction system containing 200 nM T_{DNA}, 1 μM H_1 and 1 μM H_2. Native PAGE was used to analyze different component combinations. T_{DNA} (Lane 1), H_1 (Lane 2), and H_2 (Lane 3) exhibited a single distinct band, respectively. Upon incubation of T_{DNA}, H_1, and H_2 at 37 °C for 2 h (Lane 4), a prominent high-molecular-weight band corresponding to the H_1–H_2–T_{DNA} ternary complex was observed along with a faster migrating band attributed to the H_1–H_2 duplex formed after T_{DNA} release. Due to the excess of H_1 and H_2, residual free hairpin bands remained visible. No new bands appeared in the T_{DNA}/H_1 mixture (Lane 5), indicating the absence of nonspecific hybridization. In contrast, the T_{DNA}/H_2 mixture (Lane 6) showed a faint additional band, likely resulting from limited sequence complementarity and prolonged incubation. The H_1/H_2 mixture (Lane 7) predominantly displayed individual hairpin bands, with only a very weak H_1–H_2 duplex band, suggesting minimal nonspecific interaction.

With the increasing concentration of target *B. pseudomallei* DNA from 1.0 fM to 1.0 nM, the photocurrent signal decreased (Fig. 4A), indicating the feasibility of the proposed "on-off" PEC detection method. Systematic optimization for the synthesis of In_2O_3/Bi_2WO_6 and the formation of DNAzyme-MB were conducted by examining the effects of experimental conditions on photocurrent response of In_2O_3/Bi_2WO_6/ITO or analytical performance of the PEC biosensor at 1.0 nM target DNA. The InO/BWO-4 prepared with an In_2O_3:Bi_2WO_6 molar ratio of 1:1.5 showed the maximum photocurrent signal (Fig. S4), and the H_2-connected MB prepared with 0.2 μM H_2 resulted in the maximum photocurrent change (Fig. S5A). The higher amount of H_2 on MBs reduced the formation rate of DNA enzyme, causing the decrease of photocurrent change. The CHA time was optimized to be 2 h (Fig. S5B).

3.5. Analytical performance of proposed PEC biosensing method

The plot of photocurrent change vs the logarithm of *B. pseudomallei* DNA concentration showed a linear correlation (R^2 = 0.9841) (Fig. 4B). The regression equation was ΔI (μA) = 0.487 + 0.061lgC_{TDNA}, where $\Delta I = I_0 - I$, I_0 represented the photocurrent of In_2O_3/Bi_2WO_6/ITO, and I represented the photocurrents of the biosensor at different concentrations of target DNA. The detection limit (LOD) was calculated from this equation using the value of blank plus 3 times the standard deviation to be 0.17 fM. Compared with previously reported CHA-based bacterial DNA detection methods and existing strategies for *B. pseudomallei* DNA detection (Table S2), the proposed detection method demonstrated superior performance in terms of detection limit and linear range. The

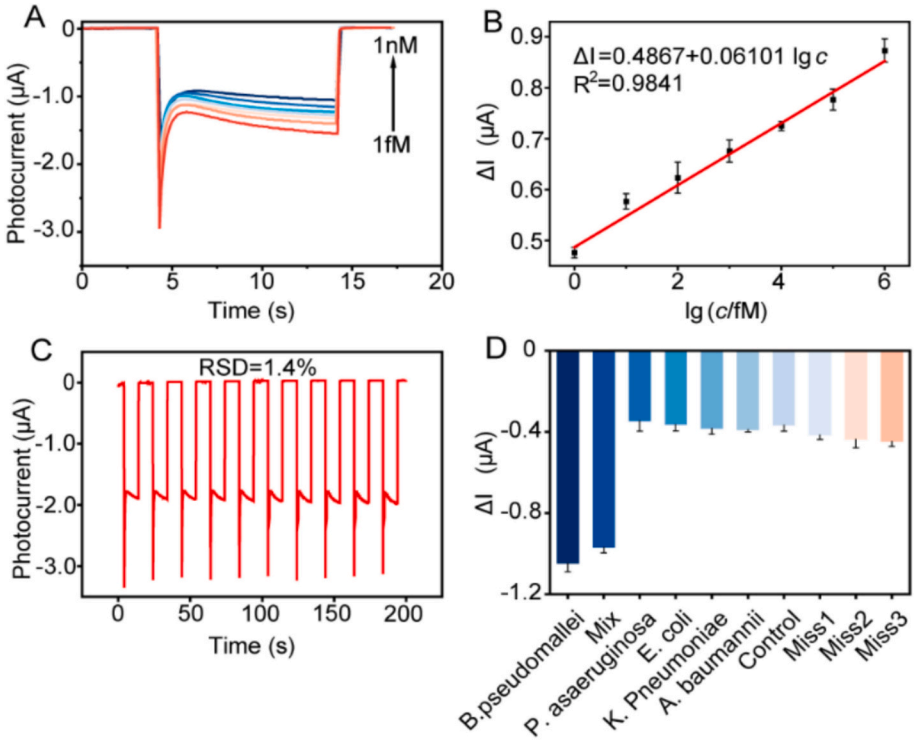

Fig. 4. (A) Photocurrent responses of the proposed biosensor to 1.0 fM-1.0 nM T_{DNA}. (B) Corresponding calibration curve. (C) Stability test of the biosensor. (D) Specificity of the proposed biosensor for T_{DNA} in comparison to other bacteria DNAs and three single-base–mismatched *B. pseudomallei* DNA at 1.0 nM.

enhanced performance could be attributed to following factors. Firstly, the CHA provided sustained nucleic acid signal amplification, enabling efficient recognition of the target DNA even at low concentrations. Secondly, the In_2O_3/Bi_2WO_6 heterojunction material improved charge separation and photogenerated electron transport, thereby enhancing the signal response during the PEC measurement. In addition, the target-triggered G-quadruplex/hemin structure catalyzed the conversion of 4-CN to 4-CD, which in turn suppressed the photocurrent at the electrode interface, making the signal differences more distinguishable. The stability testing showed consistent photocurrent responses over 10 consecutive "on–off" illumination cycles, in which each cycle consisted of 10 s of light irradiation followed by 10 s without illumination. During the measurement, the photocurrent remained highly stable, yielding a relative standard deviation (RSD) of 1.4 % (Fig. 4C), demonstrating the excellent operational stability of the sensor. The selectivity of the proposed PEC method was evaluated with DNAs from *P. aeruginosa*, *A. baumannii*, *K. pneumoniae*, *E. coli*, and three single-base–mismatched *B. pseudomallei* DNA sequences, while 1.0 nM *B. pseudomallei* DNA served as the target. This system exhibited distinct photocurrent differences when detecting single interfering DNA, blank control, target DNA alone, or the mixture of interferents and target DNA (Fig. 4D). The results did not show significant signal change for non-target DNA or blank samples, whereas the presence of target DNA caused a marked decrease in photocurrent, proving the superior selectivity and interference resistance.

3.6. Analysis of T_{DNA} in human serum samples

To further validate the practical applicability of the developed biosensing method, different concentrations of *B. pseudomallei* DNA were spiked in 100-fold diluted human serum samples obtained from Jiangsu Cancer Hospital. This dilution factor was selected to effectively minimize matrix interference from serum components while maintaining the target DNA concentration within the detectable range, as commonly adopted in related serum-based analytical studies [40–42]. The recoveries obtained using different biosensors for 10, 100, 1000, 1.0×10^4 and 1.0×10^5 fM T_{DNA} ranged from 91.4 % to 108.5 % with RSD less than 6.08 % ($n = 3$) (Table S3). These results demonstrated the satisfactory reproducibility of the biosensors, and acceptable accuracy and precision of the biosensing method, underscoring its strong promise for clinical application.

4. Conclusion

In summary, we have successfully synthesized an In_2O_3/Bi_2WO_6 heterojunction as a stable and easily assembled functional module for sensitive photoelectrochemical detection of *B. pseudomallei* DNA. Incorporating rod-like In_2O_3 into sheet-like Bi_2WO_6 facilitates the photogenerated electron transfer and enhances charge carrier separation, thus leading to 5-fold stronger PEC signal for high-performance "on-off" biosensing. By target DNA-triggered formation of abundant DNAzymes with a CHA cascade amplification for catalyzing the conversion of 4-CN to insoluble 4-CD precipitates, the proposed "on-off" biosensing method demonstrates a wide linear detection range of 1.0 nM to 1.0 fM and a detection limit of sub-femtomolar level, enabling highly sensitive detection of pathogenic DNA at early stages. This method integrating CHA strategy shows excellent selectivity and stability, and the preparation of In_2O_3/Bi_2WO_6 material is also low-cost and relatively easy, indicating promising potential for practical application. However, in practical clinic application, complex biological matrices contain abundant non-target species, which may induce non-specific adsorption and affect the background. Additionally, environmental parameters including pH, temperature, and ionic strength can influence interfacial charge distribution and electron-transfer kinetics, resulting in signal change. Thus, the PEC measurements must be carried out in PBS by spiking the samples with appropriate dilution. Future work may prioritize the development of antifouling surface strategies, such as functional coatings or molecularly imprinted polymers, to suppress non-specific binding and enhance operational robustness. By integrating microfluidic or flow-injection technology, this proposed method can achieve automated electrochemical measurement modules for real-time signal acquisition and data analysis. Coupling the sensing interface with portable readout units, smartphone-based systems, or wearable devices also enables true point-of-care applicability.

CRediT authorship contribution statement

Ye Zhao: Writing – original draft, Validation, Formal analysis, Data curation, Conceptualization. **Yiyong Wang:** Validation, Data curation. **Chen Yuan:** Investigation. **Yu Xiao:** Investigation, Formal analysis. **Qianfeng Xia:** Writing – review & editing, Supervision. **Huangxian Ju:** Writing – review & editing, Supervision, Project administration, Funding acquisition.

Declaration of competing interest

The authors declare that they have no known competing financial interests or personal relationships that could have appeared to influence the work reported in this paper.

Acknowledgements

This study was supported by National Natural Science Foundation of China (21890741, 21827812).

Appendix A. Supplementary data

Supplementary data to this article can be found online at https://doi.org/10.1016/j.microc.2026.116819.

Data availability

No data was used for the research described in the article.

References

[1] V. Suttisunhakul, V. Wuthiekanun, P.J. Brett, S. Khusmith, N.P.J. Day, M. N. Burtnick, D. Limmathurotsakul, N. Chantratitaa, Development of rapid enzyme-linked immunosorbent assays for detection of antibodies to *Burkholderia pseudomallei*, J. Clin. Microbiol. 54 (2016) 1259–1268, https://doi.org/10.1128/jcm.02856-15.

[2] I. Gassiep, M. Armstrong, R. Norton, Human melioidosis, Clin. Microbiol. Rev. 33 (2020) e00006–e00019, https://doi.org/10.1128/cmr.00006-19.

[3] N.J. White, Melioidosis, Lancet 361 (2003) 1715–1722, https://doi.org/10.1016/S0140-6736(03)13374-0.

[4] T.J.J. Inglis, J.L. Sagripanti, Environmental factors that affect the survival and persistence of *Burkholderia pseudomallei*, Appl. Environ. Microbiol. 72 (2006) 6865–6875, https://doi.org/10.1128/AEM.01036-06.

[5] J. Yao, Z. Zhang, H. Pei, T. Zhang, Y.P. Ruan, C.Y. Liu, Y.C. Guo, S. Gu, Q.F. Xia, Magnetically modified bacteriophage-triggered ATP release activated EXPAR-CRISPR/Cas14a system for visual detection of *Burkholderia pseudomallei*, Biosens. Bioelectron. 257 (2024) 116334, https://doi.org/10.1016/j.bios.2024.116334.

[6] P. Phokrai, W. Karoonboonyanan, N. Thanapattarapairoj, C. Promkong, A. Dulsuk, S. Koosakulnirand, S. Canovali, N. Indrawattana, Y. Jutrakul, V. Wuthiekanun, D. Limmathurotsakul, P.J. Brett, M.N. Burtnick, G. Lertmemongkolchai, N. Chantratita, A rapid immunochromatography test based on Hcp1 is a potential point-of-care test for serological diagnosis of melioidosis, J. Clin. Microbiol. 56 (2018), https://doi.org/10.1128/jcm.00346-18 e00346–18.

[7] D.A.B. Dance, D. Limmathurotsakul, Global burden and challenges of melioidosis, Trop. Med. Infect. Dis. 3 (2018) 13, https://doi.org/10.3390/tropicalmed3010013.

[8] D. Limmathurotsakul, N. Golding, D.A.B. Dance, J.P. Messina, D.M. Pigott, C. L. Moyes, D.B. Rolim, E. Bertherat, N.P.J. Day, S.J. Peacock, S.I. Hay, Predicted global distribution of *Burkholderia pseudomallei* and burden of melioidosis, Nat. Microbiol. 1 (2016) 15008, https://doi.org/10.1038/nmicrobiol.2015.8.

[9] B.J. Currie, M. Mayo, L.M. Ward, M. Kaestli, E.M. Meumann, J.R. Webb, C. Woerle, R.W. Baird, R.N. Price, C.S. Marshall, A.P. Ralph, E. Spencer, J. Davies, S. E. Huffam, S. Janson, S. Lynar, P. Markey, V.L. Krause, N.M. Anstey, The Darwin prospective melioidosis study: a 30-year prospective, observational investigation, Lancet Infect. Dis. 21 (2021) 1737–1746, https://doi.org/10.1016/S1473-3099(21)00022-0.

[10] D. Limmathurotsakul, K. Jamsen, A. Arayawichanont, J.A. Simpson, L.J. White, S. J. Lee, V. Wuthiekanun, N. Chantratita, A. Cheng, N.P.J. Day, C. Verzilli, S. J. Peacock, Defining the true sensitivity of culture for the diagnosis of melioidosis using bayesian latent class models, PLoS One 5 (2010) e12485, https://doi.org/10.1371/journal.pone.0012485.

[11] B.F. Xu, J. Zhang, A.P. Tanjung, F. Xu, A.J. Wang, L.P. Mei, P. Song, J.J. Feng, MOF-derived sandwich-structured dual Z-scheme $Co_9S_8/ZnIn_2S_4$/CdSe hollow nanocages heterojunction: target-induced ultrasensitive photoelectrochemical sensing of chlorpyrifos, Biosens. Bioelectron. 257 (2024) 116324, https://doi.org/10.1016/j.bios.2024.116324.

[12] N. Hai, H. Yi, Y.N. Bai, L.Y. Zhang, H.N. Chi, J.J. Yan, L.S. Zhao, S. Cai, HOF-derived step-scheme FJU-200/CdSe heterojunction: a photoelectrochemical sensing platform for sensitive detection of EGFR, Biosens. Bioelectron. 267 (2025) 116862, https://doi.org/10.1016/j.bios.2024.116862.

[13] X.B. Chen, S.H. Shen, L.J. Guo, S.S. Mao, Semiconductor-based photocatalytic hydrogen generation, Chem. Rev. 110 (2010) 6503–6570, https://doi.org/10.1021/cr1001645.

[14] X. Zhu, Y. Jia, Y. Liu, J. Xu, H. He, S. Wang, Y. Shao, Y. Zhai, Y. Zhu, Enhancing built-in electric fields via molecular symmetry modulation in supramolecular photocatalysts for highly efficient photocatalytic hydrogen evolution, Angew. Chem. Int. Ed. 63 (2024) e202405962, https://doi.org/10.1002/anie.202405962.

[15] J.R. Ran, H.P. Zhang, S.J. Fu, M. Jaroniec, J.Q. Shan, B.Q. Xia, Y. Qu, J.T. Qu, S. M. Chen, L. Song, J.M. Cairney, L.Q. Jing, S.Z. Qiao, $NiPS_3$ ultrathin nanosheets as versatile platform advancing highly active photocatalytic H_2 production, Nat. Commun. 13 (2022) 4600, https://doi.org/10.1038/s41467-022-32256-6.

[16] P. Ju, P. Wang, B. Li, H. Fan, S.Y. Ai, D. Zhang, Y. Wang, A novel calcined Bi_2WO_6/$BiVO_4$ heterojunction photocatalyst with highly enhanced photocatalytic activity, Chem. Eng. J. 236 (2014) 430–437, https://doi.org/10.1016/j.cej.2013.10.001.

[17] X.Z. Feng, R.J. Zheng, C.Y. Gao, W.F. Wei, J.G.L. Peng, R.H. Wang, S.H. Yang, W. S. Zou, X.Y. Wu, Y.F. Ji, H. Chen, Unlocking bimetallic active sites via a desalination strategy for photocatalytic reduction of atmospheric carbon dioxide, Nat. Commun. 13 (2022) 2146, https://doi.org/10.1038/s41467-022-29671-0.

[18] T. Chen, L.Z. Liu, C. Hu, H.W. Huang, Recent advances on Bi_2WO_6-based photocatalysts for environmental and energy applications, Chin. J. Catal. 42 (2021) 1413–1438, https://doi.org/10.1016/S1872-2067(20)63769-X.

[19] A. Elaouni, M.E. Ouardi, A. BaQais, M. Arab, M. Saadi, H.A. Ahsaine, Bismuth tungstate Bi_2WO_6: a review on structural, photophysical and photocatalytic properties, RSC Adv. 13 (2023) 17476–17494, https://doi.org/10.1039/D3RA01987J.

[20] J.D. Hu, D.Y. Chen, Z. Mo, N.J. Li, Q.F. Xu, H. Li, J.H. He, H. Xu, J.M. Lu, Z-scheme 2D/2D heterojunction of black phosphorus/monolayer Bi_2WO_6 nanosheets with enhanced photocatalytic activities, Angew. Chem. Int. Ed. 58 (2019) 2073–2077, https://doi.org/10.1002/anie.201813417.

[21] Y. Zang, L.J. Gong, L.Q. Mei, Z.J. Gu, Q. Wang, Bi_2WO_6 semiconductor nanoplates for tumor radiosensitization through high-Z effects and radiocatalysis, ACS Appl. Mater. Interfaces 11 (2019) 18942–18952, https://doi.org/10.1021/acsami.9b03636.

[22] L. Wang, Z.Q. Wang, L.L. Zhang, C. Hu, Enhanced photoactivity of Bi_2WO_6 by iodide insertion into the interlayer for water purification under visible light, Chem. Eng. J. 352 (2018) 664–672, https://doi.org/10.1016/j.cej.2018.07.028.

[23] F. Bakhnooh, M. Arvand, A novel photoelectrochemical approach with "signal-off" pattern for anodic detection of sunset yellow in food samples based on Bi_2WO_6/TiO_2 NTAs heterostructure nanocomposite, Food Chem. 438 (2024) 138070, https://doi.org/10.1016/j.foodchem.2023.138070.

[24] M. Amiri, K. Dashtian, M. Ghaedi, S. Mosleh, A dual surface inorganic molecularly imprinted Bi_2WO_6-CuO/Ag_2O heterostructure with enhanced activity-selectivity towards the photocatalytic degradation of target contaminants, Photochem. Photobiol. Sci. 19 (2020) 943–955, https://doi.org/10.1039/D0PP00008F.

[25] D.J. Wang, C. Wang, Q. Zhao, L. Guo, X. Yang, J. Wu, F. Fu, Au nanoparticles (NPs) surface plasmon resonance enhanced photocatalytic activities of Au/Bi_2WO_6 heterogeneous nanostructures, J. Inorg. Mater. 33 (2018) 659–666, https://doi.org/10.15541/jim20170376.

[26] Y. Jing, A.D. Fan, J.X. Guo, T. Shen, S.D. Yuan, Y.H. Chu, Synthesis of an ultrathin MnO_2 nanosheet-coated Bi_2WO_6 nanosheet as a heterojunction photocatalyst with enhanced photocatalytic activity, Chem. Eng. J. 429 (2022) 132193, https://doi.org/10.1016/j.cej.2021.132193.

[27] Z.Q. Li, X.T. Chen, Z.L. Xue, Microwave-assisted synthesis and photocatalytic properties of flower-like Bi_2WO_6 and Bi_2O_3–Bi_2WO_6 composite, J. Colloid Interface Sci. 394 (2013) 69–77, https://doi.org/10.1016/j.jcis.2012.12.002.

[28] J. Michel, D. Splith, J. Rombach, A. Papadogianni, T. Berthold, S. Krischok, M. Grundmann, O. Bierwagen, H. Wenckstern, M. Himmerlich, Processing strategies for high-performance Schottky contacts on n-type oxide semiconductors: insights from In_2O_3, ACS Appl. Mater. Interfaces 11 (2019) 27073–27087, https://doi.org/10.1021/acsami.9b06455.

[29] H. Xu, S.C. Chen, K. Wang, X.T. Wang, Enhancing the PEC water splitting performance of In_2O_3 nanorods by a wet chemical reduction, Int. J. Hydrog. Energy 47 (2022) 38219–38228, https://doi.org/10.1016/j.ijhydene.2022.08.305.

[30] G.J. Chen, Y. Qin, L. Jiao, J.J. Huang, Y. Wu, L.Y. Hu, W.L. Gu, D.C. Xu, C.Z. Zhu, Nanozyme-activated synergistic amplification for ultrasensitive photoelectrochemical immunoassay, Anal. Chem. 93 (2021) 6881–6888, https://doi.org/10.1021/acs.analchem.1c01217.

[31] R.J. Zeng, H.X. Gong, Y.L. Li, Y.X. Li, W. Lin, D.P. Tang, D. Knopp, CRISPR-Cas12a-derived photoelectrochemical biosensor for point-of-care diagnosis of nucleic acid, Anal. Chem. 94 (2022) 7442–7448, https://doi.org/10.1021/acs.analchem.2c01373.

[32] W.W. Zhao, P.P. Yu, J.J. Xu, H.Y. Chen, Ultrasensitive photoelectrochemical biosensing based on biocatalytic deposition, Electrochem. Commun. 13 (2011) 495–497, https://doi.org/10.1016/j.elecom.2011.02.031.

[33] X. Huang, Q.Y. Lin, L.L. Lu, M.J. Li, D.P. Tang, In_2O_3/$CdIn_2S_4$ heterojunction-based photoelectrochemical immunoassay of carcinoembryonic antigen with enzymatic biocatalytic precipitation for signal amplification, Anal. Chim. Acta 1228 (2022) 340358, https://doi.org/10.1016/j.aca.2022.340358.

[34] M.S. Liu, X.Y. Sun, W.Q. Li, K.Q. Gao, Y.W. Li, F.S. Liu, M.B. Wu, Insight into synergistic catalysis of core-shell ZIF-8/ In_2O_3 hollow nanocomposite for efficient atmospheric CO_2 fixation, AICHE J. 71 (2025) e70020, https://doi.org/10.1002/aic.70020.

[35] J.Q. Tian, Y.Y. Zhang, Z.H. Shi, Z.Y. Liu, Z.W. Zhao, J. Li, N. Li, H.W. Huang, Enabling interfacial lattice matching by selective epitaxial growth of CuS crystals on Bi_2WO_6 nanosheets for efficient CO_2 photoreduction into solar fuels, Angew. Chem. Int. Ed. 64 (2025) e202418496, https://doi.org/10.1002/anie.202418496.

[36] M.L. Myrick, M.N. Simcock, M. Baranowski, H. Brooke, S.L. Morgan, J. N. McCutcheon, The Kubelka-Munk diffuse reflectance formula revisited, Appl. Spectrosc. Rev. 46 (2011) 140–165, https://doi.org/10.1080/05704928.2010.537004.

[37] C.C. Chu, W. Miao, Q.J. Li, D.D. Wang, Y. Liu, S. Mao, Highly efficient photocatalytic H_2O_2 production with cyano and SnO_2 co-modified g-C_3N_4, Chem. Eng. J. 428 (2022) 132531, https://doi.org/10.1016/j.cej.2021.132531.

[38] Z.J. Zhu, H.W. Huang, L.Z. Liu, F. Chen, N. Tian, Y.H. Zhang, H. Yu, Chemically bonded α-Fe_2O_3/Bi_4MO_8Cl dot-on-plate Z-scheme junction with strong internal electric field for selective photo-oxidation of aromatic alcohols, Angew. Chem. Int. Ed. 61 (2022) e202203519, https://doi.org/10.1002/anie.202203519.

[39] Q. Wu, Y.N. Liu, H.C. Jing, H.B. Yu, Y. Lu, M.X. Huo, H.L. Huo, Peculiar synergetic effect of γ-Fe_2O_3 nanoparticles and graphene oxide on MIL-53 (Fe) for boosting photocatalysis, Chem. Eng. J. 390 (2020) 124615, https://doi.org/10.1016/j.cej.2020.124615.

[40] L.M. Guo, Q. Zhao, Determination of the platelet-derived growth factor BB by a competitive thrombin-linked aptamer-based Fluorometric assay, Microchim. Acta 183 (2016) 3229–3235, https://doi.org/10.1007/s00604-016-1978-1.

[41] D.B. Zhang, Y.Q. Guo, L. Xiao, S.Z. Pu, A highly sensitive 'turn-on' phosphorescence probe based on iridium (III) complex with polyether segment subunits for rapid detection of thiophenol, Organomet. Chem. 928 (2020) 121551, https://doi.org/10.1016/j.jorganchem.2020.121551.

[42] J.D. Lu, D. Spasic, F. Delport, T.V. Stappen, I. Detrez, D. Daems, S. Vermeire, A. Gils, J. Lammertyn, Immunoassay for detection of infliximab in whole blood using a fiber-optic surface plasmon resonance biosensor, Anal. Chem. 89 (2017) 3664–3671, https://doi.org/10.1021/acs.analchem.6b05092.